Tailored Electrospinning of WO₃ Nanobelts as Efficient Ultraviolet Photodetectors with Photo-Dark Current Ratios up to 1000

Zhiyang He,[†,‡] Qiao Liu,[‡] Huilin Hou,[‡] Fengmei Gao,[‡] Bin Tang,*[†] and Weiyou Yang*[‡]

[†]Research Institute of Surface Engineering, Taiyuan University of Technology, Taiyuan City 030024, P. R. China
[‡]Institute of Materials, Ningbo University of Technology, Ningbo City 315016, P. R. China

ABSTRACT: In this work, polycrystalline WO₃ nanobelts were fabricated via an electrospinning process combined with subsequent air calcination. The resultant products were characterized by X-ray diffraction, field-emission scanning electron microscopy, and high-resolution transmission electron microscopy in regard to the structures. It has been found that the applied voltage during the electrospinning process played the determined role in the formation of the WO₃ nanobelts, allowing the controlled growth of the nanobelts. The ultraviolet (UV) photodetector assembled by an individual WO₃ nanobelt exhibits a high sensitivity and a precise selectivity to the different wavelength lights, with a very low dark current and typical photo-dark current ratio up to 1000, which was the highest for any WO₃ photodectectors ever reported. This work could not only push forward the facile preparation of WO₃ nanobelts but also represent, for the first time, the possibility that the polycrystalline WO₃ nanobelts could be a promising building block for the highly efficient UV photodetectors.

KEYWORDS: electrospinning, WO₃, nanobelts, polycrystalline, photodetector
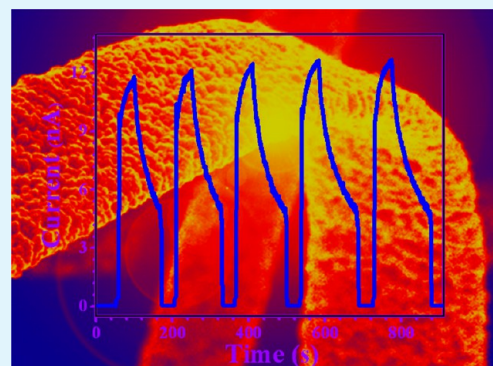
1. INTRODUCTION

Recently, the integration of functional nanodevices using semiconducting nanostructures has become an emerging requirement and a hot nanotechnology topic.[1−3] As one of the most important devices, the photodetector shows widespread applications in environmental and biological research, sensors, pollution monitoring, water sterilization, missile launch and detection, etc.[4−6] The semiconductors with wide band gaps, such as GaN, ZnO, SnO₂, etc., have been employed as ultraviolet (UV) photodetectors because of their high sensitivity and selectivity.[7−10] Among them, tungsten oxide (WO₃), as an interesting *n*-type semiconductor with outstanding electrochromic and photochromic behavior, is favorable for the applications as a photodetection candidate.[11−13]

The reported WO₃ nanostructured photodetectors were mainly based on their single-crystalline nanocounterparts,[10,14] showing they were sensitive to UV light but with limit photo-dark current ratios typically below 200. With respect to the single-crystalline nature, it permits only band-edge modulation along the radial direction. However, the energy bands are still flat along the axial direction to bring a fast track for carrier transport, which inevitably results in a large dark current due to the intrinsic carrier concentration, contradicting the performance of devices such as detectivity, noise equivalent power, linear dynamic range, etc. In contrast, the polycrystalline WO₃ counterparts might facilitate a low dark current due to the existence of much more crystalline grains and boundaries that served as the energy barriers for carrier transport, suggesting

their fascinating and wide applications in photonic devices.[15−17] However, to the best of our knowledge, no work has shed light on their applications in photodetectors.

To date, the polycrystalline WO₃ nanostructures have been prepared by thermal oxidation,[18] a template-based method combined with a particle filling technique,[19] plasma processing,[20] chemical vapor deposition (CVD),[21] atomic layer deposition (ALD),[22] the sol−gel method,[23] a hydrothermal route,[24] physical vapor deposition (PVD),[25] electrospinning,[26] etc. Among these, electrospinning is simple, versatile, and highly effective for manufacturing massive nanostructures with high aspect ratios.[27−29] However, it is still a ground challenge for electrospinning fibers with tailored morphologies, e.g., electrospinning nanobelts rather than the conventional fibers with circular cross sections.[26,29,30]

Herein, we reported the preparation of polycrystalline WO₃ nanobelts via electrospinning precursors containing polyvinylpyrrolidone (PVP) and tungsten hexachloride (WCl₆), followed by high-temperature calcination in air. Further, we demonstrated that nanobelt formation can be tailored by controlling the applied voltages (*V*), allowing their tailored growth with various cross sections. Subsequently, we investigated the performances of the photodetector assembly by the as-fabricated individual WO₃ nanobelt, showing its

wavelength selectivity, excellent stability, and high UV sensitivity with an exciting photo-dark current ratio up to 1000.

2. EXPERIMENTAL PROCEDURES

The raw materials of PVP (MW ≈ 1300000, Aladdin, Shanghai, China) and WCl_6 (99%, Aladdin, Shanghai, China) were commercially available and used directly without further purification. The precursor fibers were obtained by electrospinning the solution of polyvinylpyrrolidone (PVP) and tungsten hexachloride (WCl_6). The mixture of absolute ethyl alcohol and N,N-dimethylformamide (DMF) at a volume ratio of 1:4 was used as the solvent. First, 0.4 g of PVP was dissolved in the mixed solvent (5 mL) by vigorously stirring for 2 h. Then, 2 g of WCl_6 was added to the resultant solution while it was being magnetically stirred. The obtained solution was then transformed into a plastic syringe with a plastic nozzle as the anode. The syringe was horizontally placed with a typical fixed distance of 18 cm between the top of the nozzle and the collector (wire entanglement) that acted as the cathode. Voltages of 8−18 kV were applied between these two electrodes via a high-voltage power supply. Electrospinning was conducted under environmental conditions. The as-spun PVP/WCl_6 precursor nanofibers collected on the wire entanglement were then dried in an electric oven at 70 °C. Subsequently, the precursor nanofibers were heated to 500 °C at a heating rate of 5 °C min^{-1}, maintained there for 0.5 h in air, and cooled in a furnace to ambient temperature. To understand the mechanism of formation of WO_3 nanobelts, a series of experiments were conducted by varying the applied voltages (V), and the corresponding products were termed WO_3-V (V = 8, 10.5, 13, 15.5, and 18 kV), as shown in Table 1.

Table 1. Compositions of the Solutions and Applied Voltages for Electrospinning

sample	WCl_6 (g)	PVP (g)	DMF (mL)	ethanol (mL)	voltage (kV)
WO_3-8	2	0.8	4	1	8
WO_3-10.5	2	0.8	4	1	10.5
WO_3-13	2	0.8	4	1	13
WO_3-15.5	2	0.8	4	1	15.5
WO_3-18	2	0.8	4	1	18

The obtained products were characterized by X-ray powder diffraction (XRD, D8 Advance, Bruker) with Cu Kα radiation (λ = 1.5406 Å). The morphologies and chemical compositions of the nanofibers were examined by field emission scanning electron microscopy (FESEM) (S-4800, Hitachi) and high-resolution transmission electron microscopy (HRTEM) (JEM-2010F, JEOL) equipped with an energy-dispersive X-ray spectroscopy (EDX) instrument (Quantax-STEM, Bruker).

The resultant nanobelts of WO_3-18 were dispersed in ethanol by ultrasonic treatment for 30 min and dropped onto prefabricated gold electrodes on a Si substrate (covered with a 200 nm thick SiO_2 layer), for assembling the photodetector device. The gold electrodes had previously been cleaned successively by sonication in acetone, ethanol, and deionized water for 15 min and then dried in a nitrogen stream. Subsequently, the obtained photodetector was heat-treated at 100 °C for 1 h to volatilize the solvent completely. The current−voltage (I−V) and current−time (I−t) characteristics of the photodetectors were measured using a semiconductor characterization system (4200-SCS, Keithley). The spectroscopic responses for different wavelengths were measured by using a 500 W Ushio xenon lamp as the excitation source with an illumination bandwidth of 5 nm. The photocurrent was measured by fixing certain light wavelengths with adjustable light intensity (405 nm, P_{max} = 200 mW, with a laser spot size 4 mm in diameter). The light intensity was measured with an OAI-306 power meter. All experiments were performed at room temperature under ambient conditions.

3. RESULTS AND DISCUSSION

SEM was first employed to show the morphology of the as-spun precursors of WO_3-18 and the corresponding calcined products (Figure 1a−f). It can be seen that the resultant
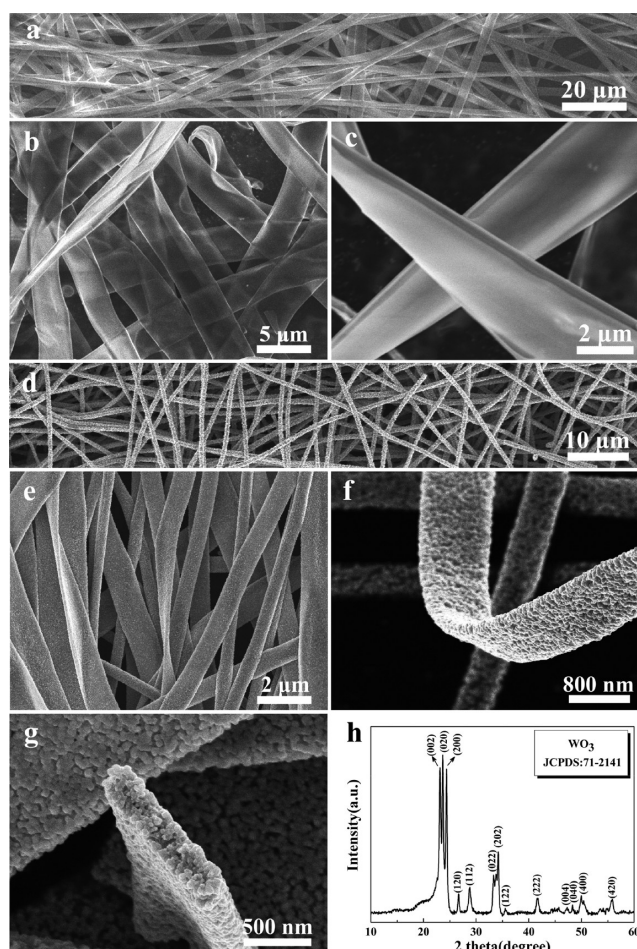

Figure 1. (a−c) Typical SEM images of the as-spun PVP/WCl_6 nanobelts of WO_3-18 at different magnifications. (d−g) Typical SEM images of the corresponding calcined products at different magnifications. (h) Representative XRD pattern recorded from sample E after calcination at 500 °C for 30 min.

precursors are highly purified nanobelts in morphologies with a typical width of 3−3.5 μm (Figure 1a,b). Closer observation (Figure 1c) discloses that the thickness of the nanobelts is representatively in the range of 200−300 nm, suggesting that the precursor nanobelts have a width/thickness (w/t) ratio of >10. These experimental results also confirm that the nanobelts with rectangular cross sections should be formed prior to the high-temperature calcination treatment. Panels d−g of Figure 1 present the typical SEM images of the corresponding calcined products. It seems that the resultant products replicate the initial profile with typical nanobelt morphology (Figure 1d,e). The width and thickness of the calcined products are typically sized as ∼1 μm and 100 nm, respectively. The shrinkage of the nanobelts, as compared to the as-spun precursor ones, could be mainly due to the elimination of PVP and the formation of crystalline WO_3 induced by the high-temperature calcination.[31] Interestingly, the bent WO_3 nanobelts could be often observed, suggesting that the as-fabricated nanobelts are somewhat flexible. The representative cross section (Figure 1g) clearly

discloses the rectangular feature of the nanobelts, which is composed of densely packed nanoparticles. Figure 1h shows the typical XRD pattern of the calcined samples. The diffractions match well with the pure phase of monoclinic WO_3 (JCPDS Card No. 71-2141), indicating the high-purity phase composition of the resultant nanobelts. The sharp diffractions suggest that they are highly crystalline.

TEM is further performed to study the structural details of the nanobelts. Panels a and b of Figure 2 present the typical
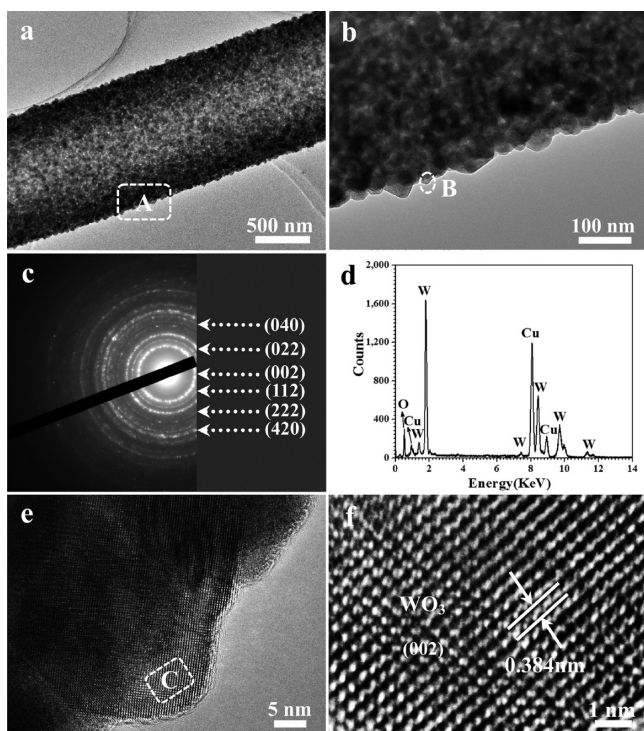

Figure 2. (a and b) Typical TEM images of a single WO_3 nanobelt of calcined sample WO_3-18 at different magnifications. (c) Typical SAED pattern recorded from the single WO_3 nanobelt recorded from marked area A in panel a. (d) Typical EDX spectrum of calcined sample WO_3-18. (e) Representative HRTEM image recorded from marked area B in panel b. (f) Enlarged HRTEM image of marked area C in panel e.

TEM images of a randomly selected nanobelt at different magnifications. It suggests that the as-fabricated WO_3 nanobelts are mechanically robust because they have been subjected to the ultrasonic treatments for TEM sample preparation. Figure 2b is the corresponding TEM image recorded from marked area A in panel a at a high magnification, disclosing that the resultant products consist of dense nanoparticles typically ~20 nm in size. Figure 2c presents the corresponding selected area electron diffraction (SAED) pattern. The diffraction spot rings suggest its polycrystalline nature with a high crystallinity. They can be sequentially indexed to (002), (112), and (022) crystal planes of monoclinic WO_3 (JCPDS Card No. 71-2141), which is in good agreement with the results of XRD analyses. The chemical composition of the obtained nanobelts is identified by EDX, revealing that the products consist mainly of W and O. The detected Cu and C signals come from the copper grid for TEM sample support. The atomic ratio of W to O, within the experimental limitation, is close to 1:3 (i.e., 8.41:23.08), confirming that the nanobelts are WO_3. Figure 2e is the HRTEM image recorded from marked area B in panel b, disclosing the single-crystalline nature of individual nano-

particles within the nanobelts. The measured d spacing between two neighbored lattice fringes is 0.384 nm (Figure 2f), corresponding to the (002) plane distance of monoclinic WO_3.

To disclose the determined role in the formation of the WO_3 nanobelts, four comparison experiments are set up by adjusting the applied spinning voltages from 8 to 18 kV, as shown in Table 1. Figure 3 shows the typical SEM images of the precursor samples and corresponding calcined samples with tailored applied spinning voltages of 8, 10.5, 13, and 15.5 V at different magnifications. It is clearly demonstrated that the structure evaluation of the as-spun precursor fibers and calcined counterparts with different applied voltages are both from typically circular cross section to elliptical counterparts, and finally to rectangular ones. It implies that when the applied voltage is fixed at a relatively low value of 8 kV [sample WO_3-8 (Figure 3, a_1-a_4)], the corresponding product is representatively shaped in circular cross sections, which is distinctively different from the shape of those obtained at an applied voltage of 18 kV. Interestingly, once the applied voltage increases to 10.5 kV [sample WO_3-10.5 (Figure 3, b_1-b_4)] and further to 13 kV [sample WO_3-13 (Figure 3, c_1-c_4)], the cross-section morphology of corresponding products becomes representatively elliptical. When the applied voltage rises further to 15.5 kV [sample WO_3-15.5 (Figure 3, d_1-d_4)], the resultant products appear to be beltlike nanostructures with typical rectangular cross sections. In terms of the as-fabricated products at a fixed voltage of 18 kV, which also possess the similar rectangular cross sections, it implies that the morphologies of the products maintain stable in rectangular cross section, once the spinning voltages are fixed up to 15.5 kV. These results suggest that the voltages play a critically important role in the formation of the nanobelts, which allow their growth in a controlled manner. In the case presented here, the spinning voltage should be fixed above 15.5 kV to accomplish the growth of WO_3 nanobelts. Further XRD analyses of samples WO_3-8, WO_3-10, WO_3-13, and WO_3-15 disclose that they are also pure monoclinic WO_3 (JCPDS Card No. 71-2141), which is identical to that of sample WO_3-18 (experimental setup not shown here).

The following typical process was used for the formation of fibers via electrospinning.[32] (i) The applied voltage forces the ejection of an initial liquid jet often in round shape, when it overcomes the surface tension. (ii) The as-ejected round precursor experiences a transitory movement toward the collector driven by the electrostatic field force. (iii) The spun precursor fibers are collected and solidified over the collector. On the basis of the observations of the spun polymeric precursor products with various applied voltages as mentioned above (Figure 3, a_1-d_1), we proposed a mechanism for the formation of the WO_3 nanobelts, which mainly includes three steps, spun circular fibers, collapse of the fibers, and finally formed nanobelts. In other words, the formation of the WO_3 nanobelts with a typically rectangular cross section is attributed to the collapse of the as-spun polymeric precursor fibers. This could be verified by the morphology feature often observed in the products, examples of which are samples WO_3-13 and WO_3-18 as the marked arrows in panels a and b of Figure 4, showing some of the details of the collapse for the formation of the spun precursor nanobelts. As reported by the previous works, during the movement of the spun polymeric precursor fibers to the collector, a polymer dry skin surrounding fibers is always formed caused by the evaporation of the solvents (e.g., ethanol) at the relatively higher temperature (i.e., ~40 °C in
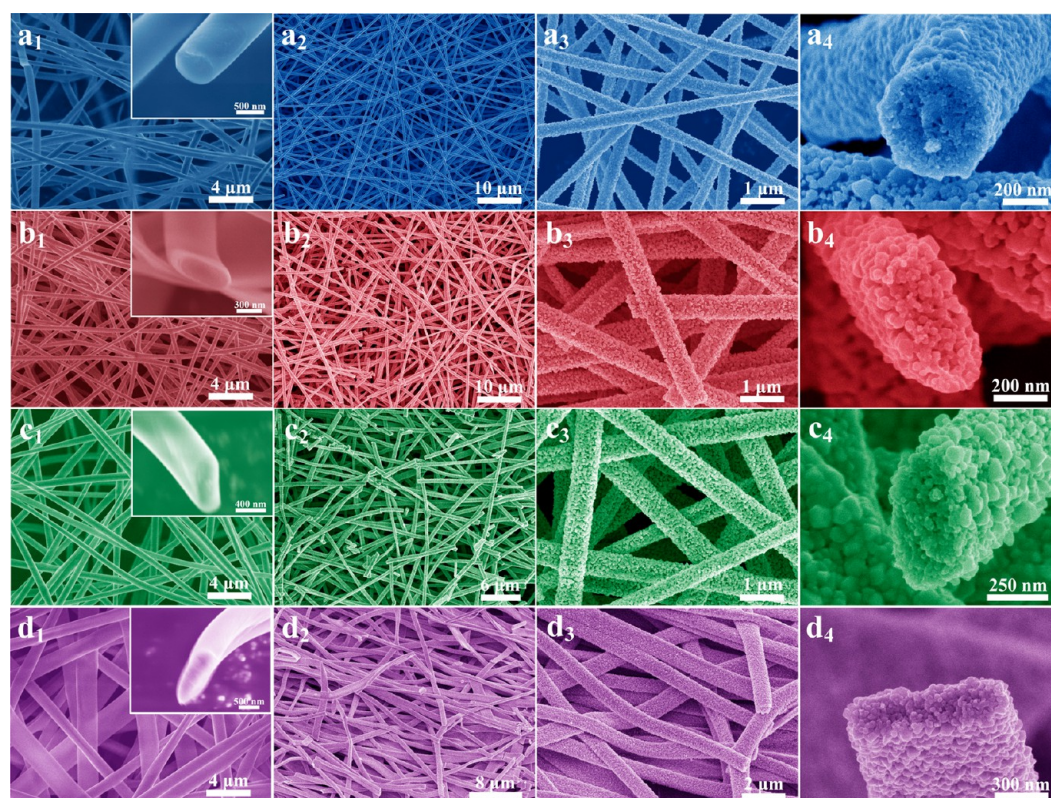
Figure 3. (a_1−d_1) Typical SEM images of the as-spun PVP/WCl$_6$ precursor fibers of samples WO$_3$-8, WO$_3$-10.5, WO$_3$-13, and WO$_3$-15.5, respectively. The insets show the typical cross sections of the four samples. (a_2−a_4) Typical SEM images of the calcined products of sample WO$_3$-8 at different magnifications. (b_2−b_4) Typical SEM images of the calcined products of sample WO$_3$-10.5 at different magnifications. (c_2−c_4) Typical SEM images of the calcined products of sample WO$_3$-13 at different magnifications. (d_2−d_4) Typical SEM images of the calcined products of sample WO$_3$-15.3 at different magnifications. The colors draw the eyes to different samples.
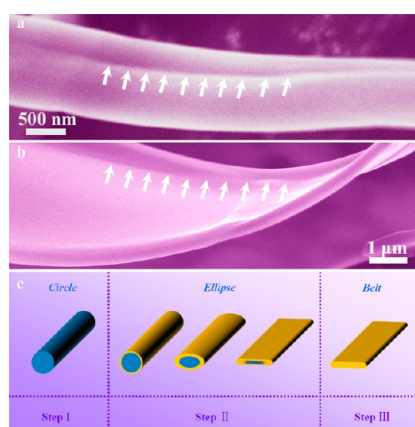

Figure 4. (a and b) Typical SEM images of as-spun PVP/WCl$_6$ precursor fibers of samples WO$_3$-13 and WO$_3$-8, respectively. The arrowheads show the collapse of the fibers. (c) Schematic illustration of the formation of WO$_3$ nanobelts.

current spinning experiments).[6,33] The various moving speeds induced by different applied voltages could result in the different evaporation times of the solvents, which finally cause the formation of the dry skins with different thicknesses around the outside layer of the fibers. Once the applied voltage was fixed at a relatively low level to 8 kV [sample WO$_3$-8 (Figure 3, a_1−a_4)], the precursor nanofibers would experience more time from the anode to the collector because of the lower electrostatic force compared to the high applied voltage of 18 kV,[34] causing the formation of a thicker dry skin. Accordingly,

when the applied voltage at a sufficiently high level up to 15.5 kV [sample WO$_3$-15.5 (Figure 3, d_1−d_4)], the precursor nanofibers would experience less time from the anode to the collector because of the greater electrostatic force, causing the formation of a thinner dry skin. Subsequently, the continuous evaporation of the inside solvent within the spun products would lead to the collapse of the polymeric precursor fiber, which depends on the thickness of the previously formed dry skins, because different thicknesses of the skins could allow them to possess various abilities against the collapse. In other words, the nanobelts with a rectangular cross section might be caused by the collapse of the spun polymer precursor fibers with preformed thinner dry skins induced by a sufficiently high applied voltage up to 15.5 kV and even a higher one [samples WO$_3$-15.5 and WO$_3$-18 (Figures 1 and Figure 3, d_1−d_4)]. The nanofibers with a circular cross section would remain stable because of its preformed thick dry skins with a sufficiently long evaporation time for the solvents induced by a low voltage of 8 kV [sample WO$_3$-8 (Figure 3, a_1−a_4)]. Once the spinning voltages are fixed between 8 and 15.5 kV, the intermediate products with the elliptical cross section could be consequently obtained [samples WO$_3$-10 and WO$_3$-13.5 (Figure 3, b_1−b_4 and c_1−c_4)], which further confirm the formation of the WO$_3$ nanobelts caused by the collapse of the as-spun circular fibers. These experimental results strongly suggest that the applied spinning voltages play a determined role on the formation of the WO$_3$ nanobelts, allowing their controlled growth of the as-spun nanofibers in the cross-section shapes.

As compared to the circular nanofibers, the nanobelts with a rectangular cross section could allow them to lie on the previously prepared microelectrodes, which could effectively bring them into face-to-face contact with the electrode and thus offer the assembled photodetector a better electric contact. Thereby, an individual nanobelt of WO$_3$-18 is then assembled with a pair of gold electrodes on a SiO$_2$/Si substrate to construct a photodetector device, which is schematically illustrated in Figure 5a with its typical SEM image as the
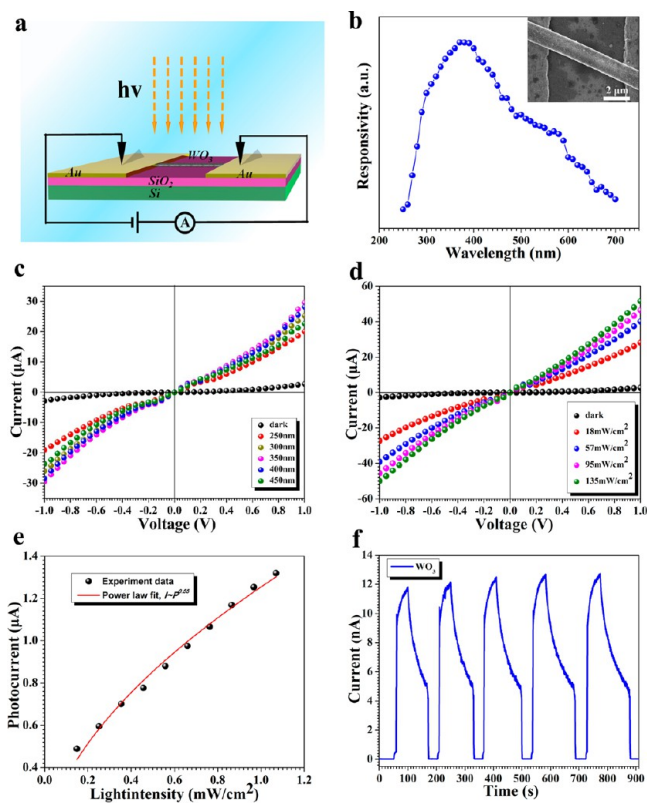

Figure 5. (a) Schematic illustration of the constructed WO$_3$ nanobelt photodetector. (b) Spectroscopic photoresponse of the photodetector measured at various wavelengths ranging from 250 to 700 nm at a bias of 1 mV. The inset shows the corresponding SEM image of the assembled WO$_3$ nanobelt photodetector. (c) I−V curves of the photodetector illuminated by the lights with different wavelengthes and in the dark. (d) I−V curves of the photodetector under 405 nm light irradiation under various intensities and dark conditions. (e) Photocurrents as a function of light intensity with the corresponding fitting curve using the power law. (f) Time response of the photodetector under 405 nm light illumination at a bias of 1 mV under atmospheric conditions.

inset in Figure 5b. Figure 5b represents the spectroscopic photoresponse of the given WO$_3$ nanobelt under the light excitation with wavelengths ranging from 250 to 700 nm. It seems that, with the decrease in the light wavelengths from 700 nm, the sensitivity of the detector is gradually enhanced and reaches its maximal value at ∼400 nm. With regard to the slight increase in the photoresponse with the long wavelength, the possible reason lies in the transition of carriers from the defect states to the conduction band, while the drop of the response on the shorter wavelength side is attributed to the enhanced absorption of high-energy photons near the surface region of the semiconductor.[35] The photocurrent gradually increases when the light wavelength increases from 250 to 400 nm and

begins to drop when the light wavelength exceeds 400 nm, implying the high selectivity of the present WO$_3$ nanobelt photodetector.

Besides the selective activities as for a promising photodetector, the good linear response to light intensities is strongly desired. Figure 5c shows the I−V curves of the WO$_3$ nanobelt photodetector illuminated by the light with various wavelengths as well as in the dark. The nolinear I−V curves indicate the Schottky contact between the sample and electrodes. The photoexcited currents are much greater than those in the dark, suggesting that the detector responds to the light with a high sensitivity. Figure 5d presents the I−V curves illuminated by a 405 nm light with different light powers from 18 to 135 mV/cm^2. It verifies that higher-intensity light accompanies a higher photocurrent, suggesting that the charge carrier photogeneration efficiency is proportional to the absorbed photon flux. The corresponding dependence of photocurrent on the light power intensity is plotted in Figure 5e, which can be fitted to a power law, $Ip \sim P^\theta$, where θ determines the response of the photocurrent to light intensity, giving a nonlinear behavior with a θ of 0.51. The nonunity exponent ($0.5 < \theta < 1$) suggests a complex process of electron−hole generation, recombination, and trapping within a semiconductor.[36] This photodetector could greatly increase the lifetime of the photogenerated carriers, because of a rather high density of trap states from the nanobelts, which consist of dense nanoparticles as the photoconductive channels. Furthermore, repeatability is one of the key parameters to determine the performances of a photodetector. Figure 5f shows the time-dependent photoresponse of the WO$_3$ nanobelt device measured by periodically turning on and off the 405 nm light at the ultralow bias voltage of 1 mV under air conditions. It seems that there is a slight shift of peak photocurrent values between the two initial repeated cycles and the following ones (∼6.9%). However, the repeated stable peak values of the photocurrents after two cycles imply the excellent stabilities of the ultraviolet detector. This discloses that the photocurrent increases first to ∼12 nA and then rapidly decreases to its initial value (12 pA) once the light is turned off, suggesting the high sensitivity of the photodetector with a photo-dark current ratio up to 1000. As summarized in Table 2, it is nearly 5 times higher than any of those of the WO$_3$ nanostructured photodetectors ever reported,[10,12,14,37] and comparable to those of the photodetectors based on other nanosemiconductors such as WS$_2$,[38] ZnO,[39] SnO$_2$,[9] and In-doped Ga$_2$O$_3$.[40]

Generally, the spectral responsivity (R_λ) and external quantum efficiency (EQE) are two critical parameters for determining the sensitivity of a photodetector.[41] R_λ is defined as the photocurrent generated per unit power of incident light on the effective area of the device with a single nanobelt, and EQE reflects the ratio of the number of charge carriers circulating in the circuit to the number of photons absorbed by the device. R_λ and EQE can be expressed as

$$R_\lambda = \frac{I_{ph}}{PS} \tag{1}$$

$$EQE = \frac{hc}{e\lambda} \times \frac{I_{ph}}{PS} \tag{2}$$

where I_{ph} is the difference between the photoexcited current and dark current, P is the incident power density irradiated on the nanobelt, and S is the irradiated area of an individual nanobelt. The calculated R_λ and EQE values of the WO$_3$

Table 2. Performance of the Typical Photodetectors Based on the Nanostructured Semiconductors

semiconductor	photodetector	dark current	photocurrent	I_{light}/I_{dark}	R_λ (A/W)	EQE (%)	ref
WO$_3$	WO$_3$ nanowire	0.1 nA (at 1 V)	17.2 nA (at 1 V)	172 (at 1 V)	–	4.6×10^5	10
	WO$_3$ nanowire	0.13 μA (at 10 V)	0.15 μA (at 10 V)	1 (at 10 V)	–	–	14
	WO$_3$–NDs/RGO^a composite	~0.02 μA (at 20 V)	~1.15 μA (at 20 V)	~50 (at 20 V)	6.4	–	12
	WO$_3$–NDs/RGO composite	~0.03 μA (at 20 V)	~0.75 μA (at 20 V)	~27 (at 20 V)	4.2	1.4×10^3	37
	polycrystal WO$_3$ nanobelt	12 pA (at 5 V)	12 nA (at 5 V)	1000 (at 5 V)	2.6×10^5	8.1×10^7	this work
other typical semiconductors	WS$_2$ nanotube	–	–	336 (at 0.5 V)	3.14	615	38
	ZnO nanowire	0.13 pA (at 1 V)	0.13 nA (at 1 V)	1000 (at 1 V)	–	–	39
	ZnO nanowire	15 pA (at 5 V)	0.28 nA (at 5 V)	18.7 (at 5 V)	–	–	42
	Au-decorated ZnO nanowire	–	–	5×10^6 (at 5 V)	–	–	39
	SnO$_2$ nanowire	19.4 nA (at 1 V)	2.1 μA (at 1 V)	108 (at 1 V)	–	1.32×10^9	9
	SnO$_2$ nanowire	30 nA (at 0.1 V)	210 nA (at 0.1 V)	7 (at 0.1 V)	–	10^4	43
	Ga$_2$O$_3$ nanobelt	–	30 pA (at 30 V)	–	~10^2	~10^4	44
	In$_2$Se$_3$ nanowire	–	–	–	~89	2.2×10^3	45
	Nb$_2$O$_5$ nanobelt	~15 pA (at 0.1 V)	51.3 pA (at 1 V)	3.3 (at 1 V)	15.2	6.1×10^3	46
	In$_2$Ge$_2$O$_7$ nanobelt	–	48 nA (at 10 V)	–	3.9×10^5	2.0×10^8	47
	In-doped Ga$_2$O$_3$ nanobelt	–	91 pA (at 6 V)	910 (at 6 V)	5.5×10^2	2.72×10^5	40
	ZnS/ZnO nanobelt	0.67 μA (at 1 mV)	4.64 μA (at 1 mV)	~7 (at 1 mV)	5.5×10^5	2.0×10^8	48

^{a}WO$_3$–NDs/RGO represents WO$_3$ nanodiscs bound to reduced graphene oxide.

nanobelt presented here are as high as 2.6×10^5 A/W (comparable to the highest value ever reported, as shown in Table 2) and 8.1×10^7% (comparable to the highest value ever reported, as shown in Table 2) at an irradiation of 405 nm and a bias voltage of 1 mV, respectively. The high external quantum efficiency and responsivity indicate that the large electrical output signals such as photocurrent can be achieved with a relatively low optical input, confirming the high sensitivity of the WO$_3$ nanobelt photodetector presented here.

As for the single-crystalline nanostructure photodetectors, it is commonly accepted that the high responsivity and external quantum efficiency originate from the presence of oxygen-related hole-trap states on the nanobelt surface. These states tend to adsorb oxygen molecules from air, which favor the capture of free electrons on the nanobelt surface, namely, O$_2$(g) + e$^-$ → O$_2^-$(ad). Electron depletion at the nanobelt surface, caused by the combination of surface free electrons and oxygen molecules, leads to the formation of the space charge region and the upward band bending, as shown in Figure 6a.[49,50] Such a band bending builds an internal electric field in the radial direction, which can separate the photogenerated electron–hole pair to reduce the rate of recombination.[51] Meanwhile, the photogenerated holes migrate to the surface along the potential slope produced by band bending and participate in the surface oxygen desorption, namely, h$^+$ + O$_2^-$ → O$_2$(g), which can in turn release the captured free electrons, leading to a further increase in free electron concentration (Figure 6b).[49] These thus account for the high external quantum efficiency of single-crystalline nanostructure photodetectors. However, the core of the single-crystalline nanostructure would form the fast track for electron transport because of band bending in radial direction. Therefore, the excess free electrons would quickly migrate, which would be induced by the thermal activation without light illumination, which could result in a high dark current. As compared to the single-crystalline counterparts, the polycrystalline nanobelts possess much more crystalline grains and boundaries, which could serve as the energy barriers for carrier transport under dark condition, to suppress the dark
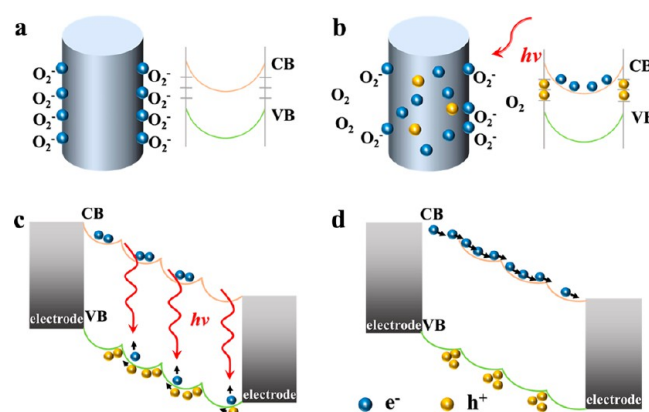

Figure 6. (a and b) Typical trapping and photoconduction mechanisms of single-crystalline WO$_3$ nanostructure without and with UV illumination, respectively. (c and d) Schematics of the carrier transport mechanism in the polycrystalline WO$_3$ nanostructure upon UV illumination.

currents of the photodetector.[4,52,53] The polycrystalline nanobelt also can acquire a high external quantum efficiency, because of a large surface area and rich surface states. At the meaning time, upon UV illumination, the excessive photogenerated holes can migrate to the grain boundaries driven by the established internal electric field to lower the barrier height. This could facilitate more free electrons easily being transported across these barriers for generating the high current upon low-intensity light illumination, as shown in panels c and d of Figure 6. This implies that the highly sensitive response of these photodetectors should contribute to the unique band-edge modulation and barrier height modulation. Meanwhile, the existence of the energy barriers leads to the highly suppressed dark current of the device,[4,52,53] further increasing the sensitivity of the photodetector. Accordingly, the enhanced photo-dark current ratio up to 1000 should be ascribed to the greatly suppressed dark current due to the abundant crystalline grains and boundaries that exist in the polycrystalline nanobelts

and the significantly increased photocurrent contributed by the unique band-edge modulation. In brief, the greatly suppressed dark current with high sensitivity of polycrystalline WO_3 nanobelt photodetectors can be achieved in our case, as compared to that of the single-crystalline counterparts.[10]

4. CONCLUSIONS

In summary, we have demonstrated a facile strategy for producing polycrystalline WO_3 nanobelts via electrospinning with subsequent air calcination. We have found that the applied voltage plays a determined role in the formation of the WO_3 nanobelts, allowing their growth in a controlled manner. The assembled WO_3 nanobelt photodetector exhibits a precise selectivity to the different wavelength lights, and a high UV sensitivity with a photo-dark current ratio up to 1000, as well as a spectral responsivity and an external quantum efficiency up to 2.6×10^5 A/W and 8.1×10^7%, respectively. This could be mainly attributed to the polycrystalline nature of the nanobelts presented here with much more crystalline grains and boundaries, as compared to the single-crystalline counterparts, which effectively suppresses the dark currents. This work could not only push forward the controlled growth of WO_3 nanobelts but also establish that the polycrystalline WO_3 nanobelts could be an excellent candidate for efficient UV photodetectors.

■ AUTHOR INFORMATION

Corresponding Authors
*E-mail: tangbin@tyut.edu.cn..
*E-mail: weiyouyang@tsinghua.org.cn. Telephone: +86-574-87080966. Fax: +86-574-87081221

Notes
The authors declare no competing financial interest.

■ ACKNOWLEDGMENTS

■ REFERENCES

(1) Li, J.; Zhou, G.; Chen, Y.; Gu, B. L.; Duan, W. Magnetism of C Adatoms on BN Nanostructures: Implications for Functional Nanodevices. *J. Am. Chem. Soc.* **2009**, *131*, 1796−1801.

(2) Mei, A.; Li, X.; Liu, L.; Ku, Z.; Liu, T.; Rong, Y.; Xu, M.; Hu, M.; Chen, J.; Yang, Y.; Grätzel, M.; Han, H. A Hole-Conductor-Free, Fully Printable Mesoscopic Perovskite Solar Cell with High Stability. *Science* **2014**, *345*, 295−298.

(3) Konstantatos, G.; Sargent, E. H. Nanostructured Materials for Photon Detection. *Nat. Nanotechnol.* **2010**, *5*, 391−400.

(4) Liu, X.; Gu, L.; Zhang, Q.; Wu, J.; Long, Y.; Fan, Z. All-Printable Band-Edge Modulated ZnO Nanowire Photodetectors with Ultra-High Detectivity. *Nat. Commun.* **2014**, *5*, 4007−4015.

(5) Tian, W.; Zhang, C.; Zhai, T.; Li, S. L.; Wang, X.; Liu, J.; Jie, X.; Liu, D.; Liao, M.; Koide, Y.; Golberg, D.; Bando, Y. Flexible Ultraviolet Photodetectors with Broad Photoresponse Based on Branched ZnS-ZnO Heterostructure Nanofilms. *Adv. Mater. (Weinheim, Ger.)* **2014**, *26*, 3088−3093.

(6) Huang, S.; Wu, H.; Zhou, M.; Zhao, C.; Yu, Z.; Ruan, Z.; Pan, W. A Flexible and Transparent Ceramic Nanobelt Network for Soft Electronics. *NPG Asia Mater.* **2014**, *6*, e86−e91.

(7) Wu, H.; Sun, Y.; Lin, D.; Zhang, R.; Zhang, C.; Pan, W. GaN Nanofibers Based on Electrospinning: Facile Synthesis, Controlled Assembly, Precise Doping, and Application as High Performance UV Photodetector. *Adv. Mater. (Weinheim, Ger.)* **2009**, *21*, 227−231.

(8) Chen, M.; Hu, L.; Xu, J.; Liao, M.; Wu, L.; Fang, X. ZnO Hollow-Sphere Nanofilm-Based High-Performance and Low-Cost Photodetector. *Small* **2011**, *17*, 2449−2453.

(9) Hu, L.; Yan, J.; Liao, M.; Wu, L.; Fang, X. Ultrahigh External Quantum Efficiency from Thin SnO_2 Nanowire Ultraviolet Photodetectors. *Small* **2011**, *7*, 1012−1017.

(10) Huang, K.; Zhang, Q.; Yang, F.; He, D. Ultraviolet Photoconductance of a Single Hexagonal WO_3 Nanowire. *Nano Res.* **2010**, *3*, 281−287.

(11) Roy Moulik, S.; Samanta, S.; Ghosh, B. Photoresponse in Thin Films of WO_3 Grown by Pulsed Laser Deposition. *Appl. Phys. Lett.* **2014**, *104*, 232107.

(12) Shao, D.; Yu, M.; Lian, J.; Sawyer, S. An Ultraviolet Photodetector Fabricated from WO_3 Nanodiscs/reduced Graphene Oxide Composite Material. *Nanotechnology* **2013**, *24*, 295701.

(13) Wang, S. J.; Lu, W. J.; Cheng, G.; Cheng, K.; Jiang, X. H.; Du, Z. L. Electronic Transport Property of Single-crystalline Hexagonal Tungsten Trioxide Nanowires. *Appl. Phys. Lett.* **2009**, *94*, 263106.

(14) Li, L.; Zhang, Y.; Fang, X.; Zhai, T.; Liao, M.; Sun, X.; Koide, Y.; Bando, Y.; Golberg, D. WO_3 Nanowires on Carbon Papers: Electronic Transport, Improved Ultraviolet-Light Photodetectors and Excellent Field Emitters. *J. Mater. Chem.* **2011**, *21*, 6525−6530.

(15) Niklasson, G. A.; Granqvist, C. G. Electrochromics for Smart Windows: Thin Films of Tungsten Oxide and Nickel Oxide, and Devices Based on These. *J. Mater. Chem.* **2007**, *17*, 127−156.

(16) Cheng, C. P.; Kuo, Y.; Chou, C. P.; Cheng, C. H.; Teng, T. P. Performance Improvement of Electrochromic Display Devices Employing Micro-Size Precipitates of Tungsten Oxide. *Appl. Phys. A: Mater. Sci. Process.* **2014**, *116*, 1553.

(17) Yan, C.; Kang, W.; Wang, J.; Cui, M.; Wang, X.; Foo, C. Y.; Chee, K. J.; Lee, P. S. Stretchable and Wearable Electrochromic Devices. *ACS Nano* **2014**, *8*, 316−322.

(18) You, G. F.; Thong, J. T. L. Thermal Oxidation of Polycrystalline Tungsten Nanowire. *J. Appl. Phys.* **2010**, *108*, 094312.

(19) Xiao, Z.; Zhang, L.; Tian, X.; Fang, X. Fabrication and Structural Characterization of Porous Tungsten Oxide Nanowires. *Nanotechnology* **2005**, *16*, 2647−2650.

(20) Moreno de Respinis, M.; De Temmerman, G.; Tanyeli, I.; van de Sanden, M. C.; Doerner, R. P.; Baldwin, M. J.; van de Krol, R. Efficient Plasma Route to Nanostructure Materials: Case Study on the Use of m-WO_3 for Solar Water Splitting. *ACS Appl. Mater. Interfaces* **2013**, *5*, 7621−7625.

(21) Hsieh, Y. T.; Chang, L. W.; Chang, C. C.; Shih, H. C. Synthesis of WO_3 Nanorods by Thermal CVD at Various Gas Flow Rates and Substrate Temperatures. *Electrochem. Solid-State Lett.* **2011**, *14*, K40−K42.

(22) Malm, J.; Sajavaara, T.; Karppinen, M. Atomic layer deposition of WO_3 thin films using $W(CO)_6$ and O_3 precursors. *Chem. Vap. Deposition* **2012**, *18*, 245−248.

(23) Solarska, R.; Alexander, B. D.; Augustynski, J. Electrochromic and Structural Characteristics of Mesoporous WO_3 Films Prepared by a Sol-Gel Method. *J. Solid State Electrochem.* **2004**, *8*, 748−756.

(24) Zhang, J.; Tu, J. P.; Xia, X. H.; Wang, X. L.; Gu, C. D. Hydrothermally Synthesized WO_3 Nanowire Arrays with Highly Improved Electrochromic Performance. *J. Mater. Chem.* **2011**, *21*, 5492−5498.

(25) Chuang, T. L.; Huang, C. L.; Gao, Y. J.; Hua, C. Y. Investigation of Microstructure, Electrical and Decorative Properties of WO_3 Film by PVD Magnetron Sputtering with Ar/O_2. *Adv. Mater. Res.* **2012**, *602−604*, 1449−1452.

(26) Wang, G.; Ji, Y.; Huang, X.; Yang, X.; Gouma, P. I.; Dudley, M. Fabrication and Characterization of Polycrystalline WO_3 Nanofibers and Their Application for Ammonia Sensing. *J. Phys. Chem. B* **2006**, *110*, 23777−23782.

(27) Agarwal, S.; Greiner, A.; Wendorff, J. H. Functional Materials by Electrospinning of Polymers. *Prog. Polym. Sci.* **2013**, *38*, 963−991.

(28) Szilágyi, I. M.; Santala, E.; Heikkilä, M.; Pore, V.; Kemell, M.; Nikitin, T.; Teucher, G.; Firkala, T.; Khriachtchev, L.; Räsänen, M.; Ritala, M.; Leskelä, M. Photocatalytic Properties of WO_3/TiO_2 Core/

Shell Nanofibers Prepared by Electrospinning and Atomic Layer Deposition. *Chem. Vap. Deposition* **2013**, *19*, 149−155.

(29) Zhao, Z. G.; Yao, Z. J.; Zhang, J.; Zhu, R.; Jin, Y.; Li, Q.-W. Rational Design of Galvanically Replaced Pt-Anchored Electrospun WO_3 Nanofibers as Efficient Electrode Materials for Methanol Oxidation. *J. Mater. Chem.* **2012**, *22*, 16514−16519.

(30) Nikfarjam, A.; Fardindoost, S.; Irajizad, A. Fabrication of Pd Doped WO_3 Nanofiber as Hydrogen Sensor. *Polymers* **2013**, *5*, 45−55.

(31) Hou, H.; Gao, F.; Wei, G.; Wang, M.; Zheng, J.; Tang, B.; Yang, W. Electrospinning 3C-SiC Mesoporous Fibers with High Purities and Well-Controlled Structures. *Cryst. Growth Des.* **2012**, *12*, 536−539.

(32) Doshi, J.; Reneker, D. H. Electrospinning Process and Applications of Electrospun Fibers. *J. Electrost.* **1995**, *35*, 151−160.

(33) Li, D.; Xia, Y. Electrospinning of Nanofibers: Reinventing the Wheel? *Adv. Mater. (Weinheim, Ger.)* **2004**, *16*, 1151−1170.

(34) Supaphol, P.; Mit-Uppatham, C.; Nithitanakul, M. Ultrafine Electrospun Polyamide-6 Fibers: Effect of Emitting Electrode Polarity on Morphology and Average Fiber Diameter. *J. Polym. Sci., Part B: Polym. Phys.* **2005**, *43*, 3699−3712.

(35) Jie, J. S.; Zhang, W. J.; Jiang, Y.; Meng, X. M.; Li, Y. Q.; Lee, S. T. Photoconductive Characteristics of Single-Crystal CdS Nanoribbons. *Nano Lett.* **2006**, *6*, 1887−1892.

(36) Kind, H.; Yan, H.; Messer, B.; Law, M.; Yang, P. Nanowire Ultraviolet Photodetectors and Optical Switches. *Adv. Mater. (Weinheim, Ger.)* **2002**, *14*, 158−160.

(37) Shao, D.; Yu, M.; Lian, J.; Sawyer, S. Ultraviolet Photodetector Fabricated from 3D WO_3 Nanowires/Reduced Graphene Oxide Composite Material. *Mater. Res. Soc. Symp. Proc.* **2014**, *1659*, 193−198.

(38) Zhang, C.; Wang, S.; Yang, L.; Liu, Y.; Xu, T.; Ning, Z.; Zak, A.; Zhang, Z.; Tenne, R.; Chen, Q. High-Performance Photodetectors for Visible and Near-Infrared Lights Based on Individual WS_2 Nanotubes. *Appl. Phys. Lett.* **2012**, *100*, 243101.

(39) Liu, K.; Sakurai, M.; Liao, M.; Aono, M. Giant Improvement of the Performance of ZnO Nanowire Photodetectors by Au Nanoparticles. *J. Phys. Chem. C* **2010**, *114*, 19835−19839.

(40) Tian, W.; Zhi, C.; Zhai, T.; Chen, S.; Wang, X.; Liao, M.; Golberg, D.; Bando, Y. In-Doped Ga_2O_3 Nanobelt Based Photodetector with High Sensitivity and Wide-Range Photoresponse. *J. Mater. Chem.* **2012**, *22*, 17984−17991.

(41) Konstantatos, G.; Sargent, E. H. Nanostructured Materials for Photon Detection. *Nat. Nanotechnol.* **2010**, *5*, 391−400.

(42) Ahn, S. E.; Ji, H. J.; Kim, K.; Kim, G. T.; Bae, C. H.; Park, S. M.; Kim, Y. K.; Ha, J. S. Origin of the Slow Photoresponse in an Individual Sol-Gel Synthesized ZnO Nanowire. *Appl. Phys. Lett.* **2007**, *90*, 153106.

(43) Lin, C. H.; Chen, R. S.; Chen, T. T.; Chen, H. Y.; Chen, Y. F.; Chen, K. H.; Chen, L. C. High Photocurrent Gain in SnO_2 Nanowires. *Appl. Phys. Lett.* **2008**, *93*, 112115.

(44) Li, L.; Auer, E.; Liao, M.; Fang, X.; Zhai, T.; Gautam, U. K.; Lugstein, A.; Koide, Y.; Bando, Y.; Golberg, D. Deep-Ultraviolet Solar-Blind Photoconductivity of Individual Gallium Oxide Nanobelts. *Nanoscale* **2011**, *3*, 1120−1126.

(45) Zhai, T.; Fang, X.; Liao, M.; Xu, X.; Li, L.; Liu, B.; Koide, Y.; Ma, Y.; Yao, J.; Bando, Y. Fabrication of High-Quality In_2Se_3 Nanowire Arrays Toward High-Performance Visible-Light Photodetectors. *ACS Nano* **2010**, *4*, 1596−1602.

(46) Fang, X.; Hu, L.; Huo, K.; Gao, B.; Zhao, L.; Liao, M.; Chu, P. K.; Bando, Y.; Golberg, D. New Ultraviolet Photodetector Based on Individual Nb_2O_5 Nanobelts. *Adv. Funct. Mater.* **2011**, *21*, 3907−3915.

(47) Li, L.; Lee, P. S.; Yan, C.; Zhai, T.; Fang, X.; Liao, M.; Koide, Y.; Bando, Y.; Golberg, D. Ultrahigh-Performance Solar-Blind Photodetectors Based on Individual Single-crystalline $In_2Ge_2O_7$ Nanobelts. *Adv. Mater. (Weinheim, Ger.)* **2010**, *22*, 5145−5149.

(48) Hu, L.; Yan, J.; Liao, M.; Xiang, H.; Gong, X.; Zhang, L.; Fang, X. An Optimized Ultraviolet-A Light Photodetector with Wide-Range Photoresponse Based on ZnS/ZnO Biaxial Nanobelt. *Adv. Mater. (Weinheim, Ger.)* **2012**, *24*, 2305−2309.

(49) Soci, C.; Zhang, A.; Xiang, B.; Dayeh, S. A.; Aplin, D. P. R.; Park, J.; Bao, X. Y.; Lo, Y. H.; Wang, D. ZnO Nanowire UV Photodetectors with High Internal Gain. *Nano Lett.* **2007**, *7*, 1003−1009.

(50) Chen, C. Y.; Retamal, J. R. D.; Wu, I. W.; Lien, D. H.; Chen, M. W.; Ding, Y.; Chueh, Y. L.; Wu, C.-I; He, J.-H. Probing Surface Band Bending of Surface-Engineered Metal Oxide Nanowires. *ACS Nano* **2012**, *6*, 9366−9372.

(51) Zhang, Z.; Yates, J. T., Jr. Band Bending in Semiconductors: Chemical and Physical Consequences at Surfaces and Interfaces. *Chem. Rev.* **2012**, *112*, 5520−5551.

(52) Hossain, F. M.; Nishii, J.; Takagi, S.; Sugihara, T.; Ohtomo, A.; Fukumura, T.; Koinuma, H.; Ohno, H.; Kawasaki, M. Modeling of Grain Boundary Barrier Modulation in ZnO Invisible Thin Film Transistors. *Phys. E (Amsterdam, Neth.)* **2004**, *21*, 911−915.

(53) Hossain, F. M.; Nishii, J.; Takagi, S.; Ohtomo, A.; Fukumura, T.; Fujioka, H.; Ohno, H.; Koinuma, H.; Kawasaki, M. Modeling and Simulation of Polycrystalline ZnO Thin-Film Transistors. *J. Appl. Phys.* **2003**, *94*, 7768−7777.